A Numerical Investigation of the Nonlinear Flow and Heat Transfer Mechanism in Rough Fractured Rock Accounting for Fluid Phase Transition Effects

Xianshan Liu [1,2,3,*], Xiaolei Luo [1], Shaowei Liu [4], Pugang Zhang [4], Man Li [1,2] and Yuhua Pan [1,2]

[1] School of Civil Engineering, Chongqing University, Chongqing 400045, China; xiaolei_up@163.com (X.L.); limancqu@163.com (M.L.); pan@cqu.edu.com (Y.P.)

[2] China Key Laboratory of New Technology for Construction of Cities in Mountain Area, Ministry of Education, Chongqing University, Chongqing 400045, China

[3] National Joint Engineering Research Center of Geohazards Prevention in the Reservoir Areas (Chongqing), Chongqing 400045, China

[4] Communications New Technology Development Company of Shanxi Province, Taiyuan 030012, China; 0126430@163.com (S.L.); a191031613@163.com (P.Z.)

[*] Correspondence: liuxianshan@163.com

Abstract: The study of the seepage and heat transfer law of three-dimensional rough fractures is of great significance in improving the heat extraction efficiency of underground thermal reservoirs. However, the phase transition effects of fluids during the thermal exploitation process profoundly influence the intrinsic mechanisms of fracture seepage and heat transfer. Based on the FLUENT 2020 software, single-phase and multiphase heat–flow coupling models were established, and the alterations stemming from the phase transition in seepage and heat transfer mechanisms were dissected. The results indicate that, without considering phase transition, the geometric morphology of the fractures controlled the distribution of local heat transfer coefficients, the magnitude of which was influenced by different boundary conditions. Moreover, based on the Forchheimer formula, it was found that the heat transfer process affects nonlinear seepage behavior significantly. After considering the phase transition, the fluid exhibited characteristics similar to shear-diluted fluids and, under the same pressure gradient, the increment of flow rate was higher than the increment in the linearly increasing scenario. In the heat transfer process, the gas volume percentage played a dominant role, causing the local heat transfer coefficient to decrease with the increase in gas content. Therefore, considering fluid phase transition can more accurately reveal seepage characteristics and the evolution law.

Keywords: seepage heat transfer; heat–flow coupling; nonlinear seepage; phase transition

1. Introduction

Hot dry rocks (HDRs) generally refer to subsurface rock bodies with temperatures exceeding 200 °C and burial depths exceeding 3 km [1]. Due to the substantial heat content in HDRs, they are often utilized in the development and utilization of geothermal resources. In the development process, to ensure the extraction of a viable and powerful future energy source from HDRs, enhanced geothermal systems (EGS) have come into existence [2]. In the operation of EGS, this mainly involves pumping low-temperature water into the hot rock area to facilitate heat exchange [3]. This implies that during the heat extraction process, due to significant temperature differences and efficient convective heat transfer, water in the fractures often undergoes phase transition, resulting in multiphase flow [4]. However, influenced by heat–flow coupling, fluids often exhibit significant nonlinear effects in rock fractures [5]. Therefore, a clear understanding of the nonlinear flow mechanisms and heat transfer mechanisms of multiphase fluids under phase transition effects is crucial for

simulating the movement of underground hot water, predicting temperature distribution in geothermal reservoirs, and optimizing geothermal energy development.

In the research on EGS, the working fluid was initially considered to flow and exchange heat in parallel plate fractures [6]. However, neglecting the roughness of the fracture surface can lead to significant errors in the calculation results [7]. Tsang [8] pointed out in a study that using a parallel plate model to simulate rough fractures can result in errors of one to two orders of magnitude in the calculated flow rates. Li et al. [9] also proposed through experiments that the roughness of the rock fracture surface will to some extent enhance the overall heat transfer intensity. Huang et al. [10] also suggested that without considering the roughness of the fracture, there would be significant errors in the calculation of convective heat transfer coefficients. Therefore, the process of convective heat transfer should be simulated based on the actual conditions of rough fractures.

Thus, to quantitatively describe the geometric morphology of fractures, Mandelbrot [11] proposed fractal geometry theory. Wang et al. [12], based on this theory, divided the fracture surface into first-order roughness with large-area undulations and second-order roughness with undulations only in local regions. Tian et al. [13], using the successive random accumulation method, constructed rough fractures with different fractal dimensions and standard deviations, and indicated that the overall heat transfer characteristics weaken with an increase in fractal dimension and a decrease in standard deviation. Huang et al. [14] quantified the surface morphology of fractures using the joint roughness coefficient (JRC) and conducted experimental research, indicating that the influence of fracture roughness on the heat transfer process cannot be ignored. Tatone et al. [15] and He et al. [16] proposed that the maximum apparent dip angle and root mean square of the fracture profile characterize the geometric morphology of fractures. They believed that the rougher the fracture, the greater the heat transfer. To analyze the relationship between heat transfer conditions and the local roughness of fractures, He et al. [17] adopted profile waviness to reflect the local geometric conditions of fractures and recognized that the larger the profile waviness, the smaller the local heat transfer coefficient. Through the study of heat transfer in rough fractures, parameters such as fluid injection velocity, injection temperature, initial temperature of the rock layer, crack width, confinement pressure, and wall roughness all influence the heat transfer mechanisms of fractured reservoirs [18,19]. However, limited by the development of experimental equipment, current research is generally conducted on heat transfer processes at low temperatures with a certain gap from the actual temperatures of HDRs [20,21]. Therefore, there is no phase transition of the fluid during the experimental process.

Thus, to gain a deeper understanding of the flow structure and movement characteristics of immiscible two-phase flow, Zhou et al. [22] analyzed the permeation mechanism of oil-water two phases under the influence of temperature through experimental analysis. Chen et al. [23] proved through visualization experiments and theoretical analysis that the flow geometry of fluid was controlled by the fracture geometry of the rough fracture. Some researchers [24,25] have also conducted thermo-hydrodynamic analyses of two-phase flow in heat pipes or microchannel coolers. However, constrained by the small-scale parameters of microchannels and the slip boundary at the fluid–solid coupling interface [26,27], the fluid's motion state is markedly different from that of high-temperature fractured fluid. In one study, Kiani [28] mentioned that in inclined single-walled carbon nanotubes (SWCNTs), a longitudinal magnetic field can be exploited as an effective method to control transverse vibrations of SWCNT-conveying fluids. However, in fractures of rock masses, parameters such as fracture aperture, confining pressure, and fracture roughness can induce changes in fluid flow behavior [29–31]. Therefore, in order to analyze the mechanism of flow nonlinearity, Liu et al. [32] suggested through experiments and numerical simulations that the rougher the fracture, the more likely it is that nonlinear seepage will occur. Xiong et al. conducted low-flow seepage experiments on fractures with five different roughnesses and found that the larger the fracture roughness, the smaller the critical Reynolds number, and the more pronounced the nonlinear effect [33]. Despite many achievements in multiphase

flow and heat transfer, the mechanisms of seepage and heat transfer under phase transition effects remain unclear. Therefore, it is essential to conduct further detailed research into its internal mechanisms.

In general, seepage and heat transfer processes in underground thermal reservoirs involve intricate heat–flow coupling and nonlinear mechanisms. Fluid phase transition is expected to exert a significant influence on both phenomena. Therefore, to analyze the underlying principles, based on FLUENT 2020 software, this research paper chose rough fractured rock as the research object and established single-phase and multiphase heat–flow coupling models. By comparing the differences in flow behavior and heat transfer with and without considering phase transition, we further investigated the flow mechanism and heat–flow coupling mechanism during phase transition. The aim was to explore multiphase flow and nonlinear flow laws in the process of heat–flow coupling in rough fractured rock.

2. Materials and Methods

2.1. Methodology

2.1.1. Interface Tracking in Multiphase Flows

Regarding interface tracking in multiphase flows, various methods have been proposed by scientists, such as the volume of the fluid (VOF) model [34], level set function method [35], and front track method, among others. Compared to other algorithms, the advantage of the VOF model in terms of efficiency is quite apparent. Therefore, the VOF model was employed to simulate boiling fluid in this study. In the VOF model, each phase in a cell is assigned a volume fraction, and the sum of volume fractions for all phases within the cell is equal to 1.

$$\alpha_1 + \alpha_2 = 1 \tag{1}$$

where α_1 and α_2 are the volume fractions of the liquid and gas, respectively.

Information about the distribution of phase interfaces can be directly extracted from the volume fractions. For example, when the volume fraction is 0 or 1, the computational grid is either empty or filled with liquid. After solving the volume fractions for all the grids, as the constructed phase interfaces are discontinuous, a piecewise linear method is employed to geometrically reconstruct the phase interfaces [36].

2.1.2. Heat–Flow Coupling Control Equation

In this study, the finite element software FLUENT 2020 was used to solve the control equation, considering that the HDR had extremely low permeability and assuming that the rock mass was impervious and the fluid incompressible. Figure 1 is a schematic diagram of the seepage and heat transfer process of rough fractures, which conceptually represents the heat transfer process of fluid through rough fractures. The fluid flows and transfers heat at the initial velocity V_{in} (m/s) and initial temperature T_{in} (K) from the inlet along the fracture surface with an aperture of δ (m) and flows out from the outlet at temperature T_{out} (K); the upper and lower walls are the thermostatic boundaries with a temperature of T_{wall} (K) and the left and right walls are insulated walls. The heat transfer process between multiphase fluids and rock mass follows continuity Equations (2) and (3) and N-S Equation (4).

$$\frac{\partial \alpha_1}{\partial t} + \nabla(\alpha_1 u_1) = -\frac{S_m}{\rho_1} \tag{2}$$

$$\frac{\partial \alpha_2}{\partial t} + \nabla(\alpha_2 u_2) = \frac{S_m}{\rho_2} \tag{3}$$

$$\bar{\rho}\frac{\partial u}{\partial t} + \nabla \cdot (\bar{\rho}uu) = -\nabla p + \nabla \cdot \left(\bar{\mu}\left[\nabla u + (\nabla u)^T\right] \right) + \bar{\rho}f \tag{4}$$

where S_m is the phase transition mass source term determined by the Lee mode [37]:

$$S_m = \begin{cases} C_1\alpha_1\rho_1(T - T_{sat})/T_{sat} \ , & T \geq T_{sat} \\ C_2\alpha_2\rho_2(T - T_{sat}) \ /T_{sat}, & T < T_{sat} \end{cases} \tag{5}$$

where ρ_1 and ρ_2 are the density (kg/m^3) of the liquid and gas, respectively; $\boldsymbol{u}$ and p are the velocity vector (m/s) and pressure (Pa). $\bar{\mu}$ and $\bar{\rho}$ are the average dynamic viscosity (kg/m·s) and average density (kg/m^3) of the control body. T_{sat} is the saturation temperature (K). $C_1 = C_2 = 100\ \mathrm{s}^{-1}$; $\boldsymbol{f}$ is the interfacial force source term caused by surface tension.
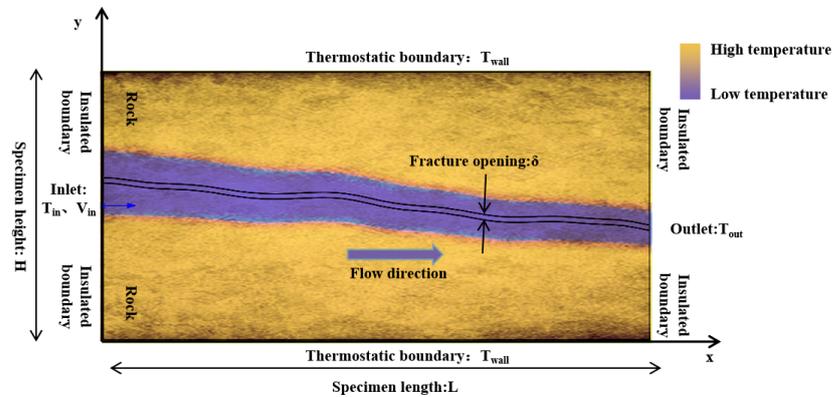
Figure 1. Conceptual diagram depicting heat transfer in rough fractures with uniform aperture.

The energy equations for rocks and fluids satisfy the following equation:

$$\nabla\bullet(-K_r\nabla T_r) = 0 \tag{6}$$

$$\frac{\partial \rho e}{\partial t} + \nabla[u(\rho e + p)] = -\nabla\bullet(k_w\nabla T_w) + S_q \tag{7}$$

In the evaporative condensation model, the phase transition energy source term S_q (W/m^3) and the specific energy of the control body e (J/kg) satisfy Equations (8) and (9):

$$S_q = h_{fg}S_m \tag{8}$$

$$\begin{cases} e = (\alpha_1\rho_1 e_1 + \alpha_2\rho_2 e_2)/(\alpha_1\rho_1 + \alpha_2\rho_2) \\ e_1 = C_{p,1}(T_w - 298.15) \\ e_2 = C_{p,2}(T_w - 298.15) \end{cases} \tag{9}$$

where K_r and T_r are the thermal conductivity (W/m·K) and contact wall temperature (K) of the rock, respectively; $C_{p,1}$ and $C_{p,2}$ are the specific heat capacity (J/kg·K) of liquid phase and gas phase water; T_w and k_w are water temperature (K) and water thermal conductivity (W/m·K), respectively; and h_{fg} is the latent heat of vaporization (J/kg) at the corresponding pressure.

It should be noted that for the single-phase heat–flow coupling model that did not consider the effect of fluid phase transition, the volume fraction and the phase transition mass source term in the control equations satisfied $\alpha_1 = 1$ and $S_m = 0$, respectively. In this case, only the liquid phase fluid was involved and there was no heat source term inside the fluid field. When the temperature of the fluid reached the saturation temperature, the temperature continued to rise without causing the phase transition phenomenon. For the multiphase heat–flow coupling model considering the effect of evaporation, the phase transition phenomenon occurred in the fluid after the temperature reached the saturation temperature. The phase transition mass source term within the fluid was no longer zero and the mass of the liquid phase fluid gradually decreased. The gas volume percentage and the mass of the gaseous phase fluid within the unit incrementally increased.

2.1.3. Convective Heat Transfer Coefficient

The convective heat transfer coefficient is a key parameter to measure the heat transfer characteristics of fluid. Many researchers derive the convective heat transfer coefficient by using Newton's cooling law and the temperature variation of the fluid after heat

absorption [38,39]. To more accurately calculate the local convective heat transfer coefficient, the fluid domain was discretized again based on the maximum grid size of 0.15 mm. As shown in Figure 2, the fluid domain was uniformly divided into four layers in the aperture direction, so the temperature of the fluid at position x is the average of the temperatures of the four layers. The temperature of the rock mass was determined by the average temperature of the upper and lower rock wall units. Finally, Equation (10) was adopted as the calculation formula for the local convective heat transfer coefficient.

$$h_{\text{local}} = \frac{\overline{C}\overline{\rho}u\delta(T_{w,x+1} - T_{w,x-1})}{2l_x\left(T_{f1,x}/2 + T_{f2,x}/2 - T_{w,x}\right)} \tag{10}$$

where δ is the aperture of the fracture (m), satisfying $\delta = 4 \times 10^{-4}$ m; $\overline{C}$ is the average specific heat capacity of the control body (J/kg·K) for the multiphase fluid, satisfying $\overline{C} = \alpha_1 C_{p,1} + \alpha_2 C_{p,2}$; $\overline{\rho}$ is the average density (m³/kg) for the multiphase fluid, satisfying $\overline{\rho} = \alpha_1 \rho_1 + \alpha_2 \rho_2$; and l_x is the length of the fluid unit, satisfying $l_x = 1.5 \times 10^{-4}$ m; $T_{w,i}$, $T_{f1,i}$ and $T_{f2,i}$ are the temperature (K) of water, the upper and lower walls at position i, respectively.
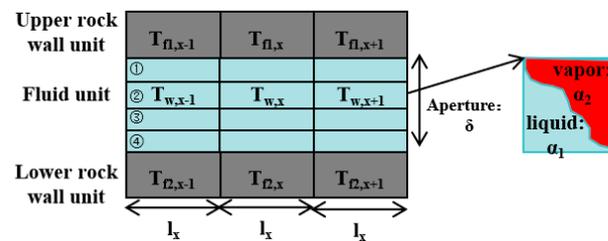
Figure 2. Schematic diagram for calculating the local convective heat transfer coefficient.

2.2. Methods

2.2.1. Construction of Single-Phase and Multiphase Heat–Flow Coupling Models

Through the Brazilian splitting test, cylindrical granite rock samples with a diameter of 50 mm and length of 100 mm were used to prepare fracture surfaces with roughness. The two split rock specimens were closed together, and a photograph of the end face was taken of them in their natural state. Then, based on the captured images, the ratio of the fracture aperture to the diameter of the rock sample was calculated. Finally, based on this ratio, the average aperture of the fracture was determined to be 0.4 mm. The geometric data of the fracture surface were obtained using a blue light 3D scanner with an accuracy of 0.01 mm. Subsequently, noise reduction and optimization processing were applied. To avoid the influence of edge damage caused by the splitting process on the fracture surface, as well as the widespread use of small-scale models in heat and transfer research [40,41], a local region of the fracture surface ($15 \leq x \leq 35, 30 \leq y \leq 70$) was divided using CAD modeling software SolidWorks 2020 (Figure 3). Next, a 3D rough fracture model with uniform apertures was constructed within this region. Finally, the geometric model was imported into Workbench Meshing for grid generation. During the meshing process, tetrahedral elements were employed to reduce discretization errors on the fracture surface. Additionally, boundary layer meshing was applied to simulate a no-slip boundary on the fracture surface, refer to Figure 4 for details. In order to obtain mesh-independent results for each specific geometric model, we determined the final number of grids of each specific geometric model by sensitivity analysis. The specific procedure involved controlling the maximum grid size in the fluid domain to obtain different numbers of grids. Subsequently, models with different numbers of grids were solved, and the temperature values at the outlet were monitored after convergence. The results for calculations with different numbers of grids are presented in Table 1. It can be observed that as the grid was further refined, the computational results eventually stabilized, but the computation

time increased. Therefore, the maximum grid size at the contact wall and within the fluid domain was ultimately controlled to be no larger than 0.15 mm.
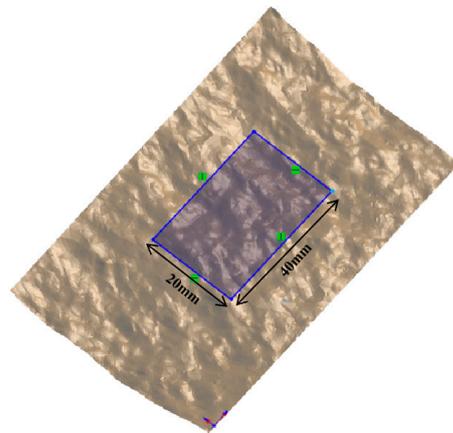
Figure 3. Model diagram of rough fracture surface.
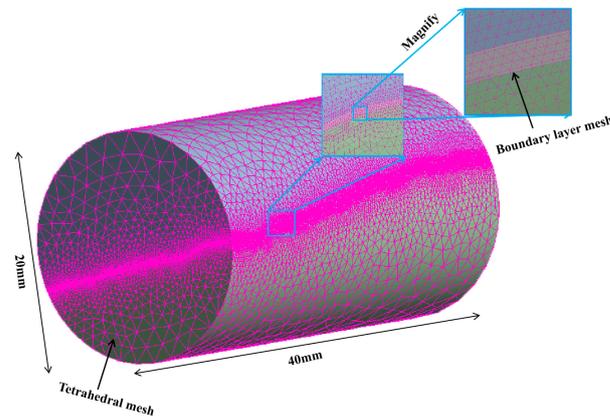
Figure 4. Model meshing diagram.

Table 1. Mesh independence validation table for the model.

Maximum Size of Grid (mm)	Number of Grids (×10⁴)	Outlet Temperature (K)	
		Single-Phase	Multiphase
2.5	33	373.870	374.165
2.2	58	368.974	369.014
1.9	90	370.042	370.634
1.5	148	369.843	370.455
1.2	170	369.851	370.435
1	230	369.850	370.437

As shown in Figure 5, the upper and lower contact surfaces between the fluid and the solid were impervious non-slip walls, i.e., $u = 0$ m/s. The front and rear walls were set as thermal insulation boundaries, i.e., $\partial T/\partial n = 0$, and the upper and lower walls were constant temperature boundaries, i.e., $T = T_{wall}$ K. The inlet of the fracture was set as a given temperature and flow rate, i.e., $T = T_{in}$.K and $u = V_{in}$ m/s, and the outlet boundary condition was set as zero pressure, i.e., $P = 0$ Pa.
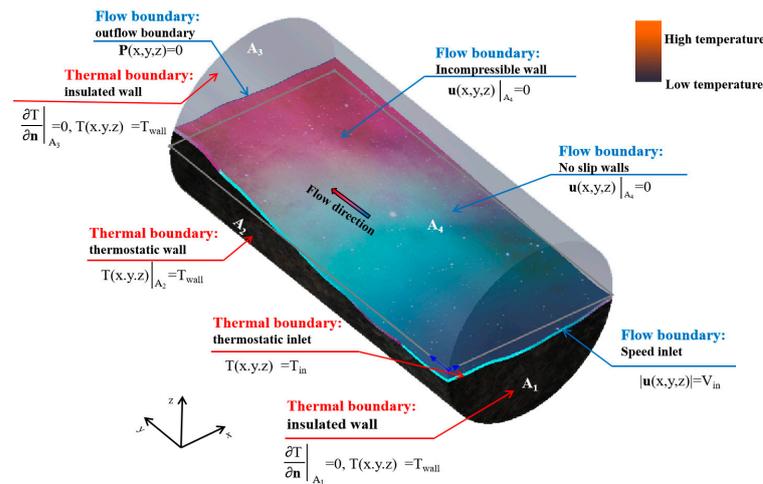
Figure 5. Schematic diagram of the initial boundary of the rough single-fracture model regarding fluid flow and heat transfer.

In the flow field region, the influence of initial fluid characteristics on the flow field and temperature field was studied by varying the inlet flow rate V_{in} and inlet temperature T_{in}, and the fluid motion state was a laminar flow. In the solid region, the influence of solid wall characteristics on the convective heat transfer effect was studied by taking the wall temperature T_{wall}. The above four variables were divided into six groups according to whether the phase transition worked, namely, V_1 and V_2 with different inlet flow rates, Ti_1 and Ti_2 with different inlet temperatures, and Tw_1 and Tw_2 at different wall temperatures, and then group Φ was set up for flow nonlinear effects, see Table 2 for specific settings. It should be noted that the single-phase and multiphase heat–flow coupling models had the same model scale, fracture surface data, grid data, and boundary conditions. The only difference was the different governing equations being solved.

Table 2. Summary of conditions for rough single-crack models.

| Group | Num | Boundary Condition | | | | Group | Num | Boundary Condition | | | |
		V_{in} (m/s)	T_{in} (K)	T_{wall} (K)	Phase Transition			V_{in} (m/s)	T_{in} (K)	T_{wall} (K)	Phase Transition
V_1	V_1–1	0.01	333.15	463.15	NO	V_2	V_2–1	0.05	333.15	463.15	YES
	V_1–2	0.03	333.15	463.15	NO		V_2–2	0.05	333.15	463.15	YES
	V_1–3	0.05	333.15	463.15	NO		V_2–3	0.05	333.15	463.15	YES
	V_1–4	0.065	333.15	463.15	NO		V_2–4	0.05	333.15	463.15	YES
	V_1–5	0.08	333.15	463.15	NO		V_2–5	0.05	333.15	463.15	YES
Ti_1	Ti_1–1	0.05	313.15	463.15	NO	Ti_2	Ti_2–1	0.05	323.15	463.15	YES
	Ti_1–2	0.05	323.15	463.15	NO		Ti_2–2	0.05	333.15	463.15	YES
	Ti_1–3	0.05	333.15	463.15	NO		Ti_2–3	0.05	343.15	463.15	YES
	Ti_1–4	0.05	343.15	463.15	NO		Ti_2–4	0.05	353.15	463.15	YES
	Ti_1–5	0.05	353.15	463.15	NO		Ti_2–5	0.05	333.15	383.15	YES
Tw_1	Tw_1–1	0.05	333.15	383.15	NO	Tw_2	Tw_2–1	0.05	333.15	383.15	YES
	Tw_1–2	0.05	333.15	403.15	NO		Tw_2–2	0.05	333.15	403.15	YES
	Tw_1–3	0.05	333.15	423.15	NO		Tw_2–3	0.05	333.15	423.15	YES
	Tw_1–4	0.05	333.15	443.15	NO		Tw_2–4	0.05	333.15	443.15	YES
	Tw_1–5	0.05	333.15	463.15	NO		Tw_2–5	0.05	333.15	463.15	YES
Φ	Φ–1	0.01	313.15	313.15	NO	Φ	Φ–4	0.065	313.15	313.15	NO
	Φ–2	0.03	313.15	313.15	NO		Φ–5	0.08	313.15	313.15	NO
	Φ–3	0.05	313.15	313.15	NO						

The physical parameters of the studied granite were set to constant and the density, specific heat capacity, and thermal conductivity were 2700 kg/m³, 920 J/(kg·K), and 1.8 W/(m·K), respectively. Since the physical parameters of the fluid changed greatly with the temperature, it was set as a function of temperature, where the density, specific heat capacity, thermal conductivity, and dynamic viscosity of the liquid phase fluid were shown in Equation (11) [42] and Equation (12) [43], respectively. The density and other physical parameters of the gas phase fluid were separately determined by Equation (13) [44] and built-in parameters (Equation (13)) in FLUENT.

$$\begin{cases} \rho_1 = 838.47 + 1.40T - 0.003T^2 + 3.72 \times 10^{-7}T^3 \\ C_{p,1} = 12010.15 - 80.41T + 0.31T^2 - 5.38 \times 10^{-4}T^3 + 3.62 \times 10^{-7}T^4 \\ k_1 = -0.87 + 0.009T - 1.58 \times 10^{-5}T^2 + 7.98 \times 10^{-9}T^3 \end{cases} \tag{11}$$

$$\mu_1 = \frac{0.01775\rho}{1 + 0.033T + 0.00021T^2} \tag{12}$$

$$\rho_2 = \begin{cases} 10^{-4}\left(0.025T^3 - 25.34T^2 + 8710.9T - 996329\right), & T \in [373.15, 423.15] \\ 10^{-4}\left(0.044T^3 - 49.2T^2 + 18865.5T - 2370607\right), & T \in [423.15, 473.15] \end{cases} \tag{13}$$

$$\begin{cases} C_{p,2} = 1563.1 + 1.60T - 0.0029T^2 + 3.22 \times 10^{-6}T^3 - 1.16 \times 10^{-9}T^4 \\ k_2 = -0.0078 + 6.81 \times 10^{-5}T + 4.49 \times 10^{-8}T^2 - 9.1 \times 10^{-12}T^3 + 6.17 \times 10^{-16}T^4 \\ \mu_2 = -4.4 \times 10^{-6} + 4.7 \times 10^{-8}T - 5.4 \times 10^{-12}T^2 + 3.2 \times 10^{-16}T^3 + 4.9 \times 10^{-22}T^4 \end{cases} \tag{14}$$

2.2.2. Verification of the Single-Phase Heat–Flow Coupling Model

In a study of seepage and heat transfer under single-phase heat–flow coupling, Bai [37] conducted seepage heat transfer experiments using a multi-field triaxial experimental system (Figure 6) developed by the Institute of Rock and Soil Mechanics, Chinese Academy of Science, to derive the overall convective heat transfer coefficient. Therefore, this paper primarily relied on the experimental data obtained by Bai [37] to conduct simulation verification. In Bai's [37] experiment, the surrounding pressure oil inside the chamber was first heated by an electromagnetic heater located outside the triaxial chamber. Then, the cylindrical granite rock sample measuring 50 × 100 mm was uniformly heated by surrounding pressure oil. When the temperature of the rock mass was consistent with the oil temperature, the pipeline was immersed at the sample inlet in high-temperature hot oil to ensure a stable fluid temperature at the inlet. Then, water was injected into the fracture at a constant flow rate by controlling the flow with an ISCO pump. Finally, temperature and pressure differences at the entrance and exit were obtained by setting sensors at the entrance and exit.
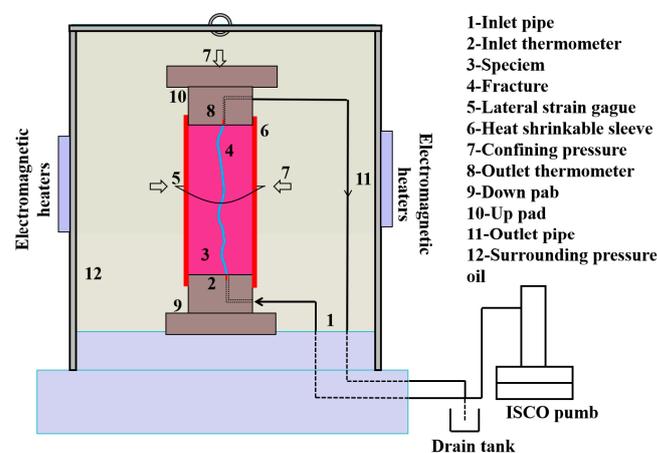
Figure 6. Schematic diagram of the multi-field triaxial test system. Source: Bai [28].

Based on the experimental research by Bai [37], 10 sets of experiments were selected for simulation verification with a temperature limit of 100 °C and a pressure limit of 0 MPa. However, due to the current experimental conditions not supporting the conduct of seepage and heat transfer experiments at high temperatures, the fluid temperature often failed to reach the saturation temperature. This limitation also prevented the occurrence of phase transition phenomena in the experiments, thereby making it impossible to obtain the corresponding experimental data. Therefore, to validate the effectiveness of the multiphase flow–heat coupling model, simulations were conducted by setting the same boundary conditions as those in the experimental conditions of Bai [37]. The specific implementation process was as follows: firstly, 3D rough fracture single-phase and multiphase flow–heat coupling models were established based on the physical parameters of the granite rock sample, and the boundary conditions of the models are shown in Figure 5. In the calculation process, the convergence condition was set as $|T_{j+1} - T_j| \leq 10^{-3} K$, where T represents the temperature at the outlet and j is the time step. For the single-phase flow–heat coupling model, the time step was set to 5×10^{-3} s. For the multiphase flow–heat coupling model, when the fluid temperature had not yet reached the saturation temperature, the time step was set to 5×10^{-3} s. Otherwise, it was adjusted to 1×10^{-3} s. The purpose of setting the time step in this way was to enhance the convergence of the model and save computational time. After setting the model parameters, computations were carried out on a computer with an Intel(R) Core(TM) i5-7300HQ processor (Lenovo, Beijing, China). For different models, the convergence time varied, with an average computation time ranging between 3 and 6 s, i.e., 1.5×10^3–6×10^3 time steps.

Figure 7 illustrates the disparities between the simulated results and the experimental outcomes. From the graph, it is evident that the simulated temperature values were higher than the measured values in the experiment. However, the maximum temperature difference between simulated and experimental values was 2.6 °C, with a relative error of 3.6%. The reasons for such discrepancies are diverse, including errors caused by the discrete process of fracture surface representation, fitting errors in the heat transfer parameters of rocks and fluids, and truncation errors during computer calculations. Referring to the simulation results from Tan [33], it can be observed that these errors fell within a reasonable range. Furthermore, from the graph, it can be observed that the outlet temperature values calculated by the two numerical models were very close. This indicates that in the absence of phase transition, the results of the multiphase flow–heat coupling model are also applicable for heat transfer research.
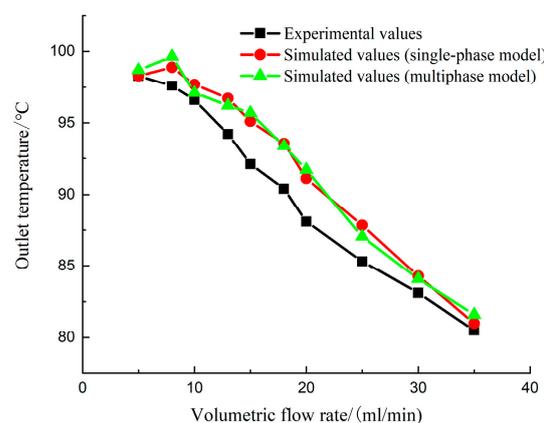
Figure 7. Comparison of numerical results and experimental results based on Bai's [28] experimental data.

3. Results and Discussion

3.1. Flow Characteristics under Single-Phase and Multiphase Flow–Thermal Coupling

Based on the established single-phase flow–heat coupling model, the fluid was added with the evaporation effect. This caused the phase transition phenomenon when the fluid

temperature reached the saturation temperature. It led to a decrease in the liquid phase fluid percentage and an increase in the gas phase volume percentage within the unit. To study the influence of the phase transition process on the flow process, the V_2, Ti_2, and Tw_2 group models considering the evaporative phenomenon and the V_1, Ti_1, and Tw_1 group models without phase transition were compared. Figure 8 shows the distribution cloud map of the gas volume percentage in the fluid domain after the exit temperature stabilized. From the figure, it can be seen that there was a distinct gas–liquid interface between the gas and liquid phases. Near the inlet, the liquid phase dominated, while near the outlet, the gas phase dominated. Because the stable temperature of the Tw_2–1 model did not reach the saturation temperature, only liquid phase fluid existed in the fluid domain.
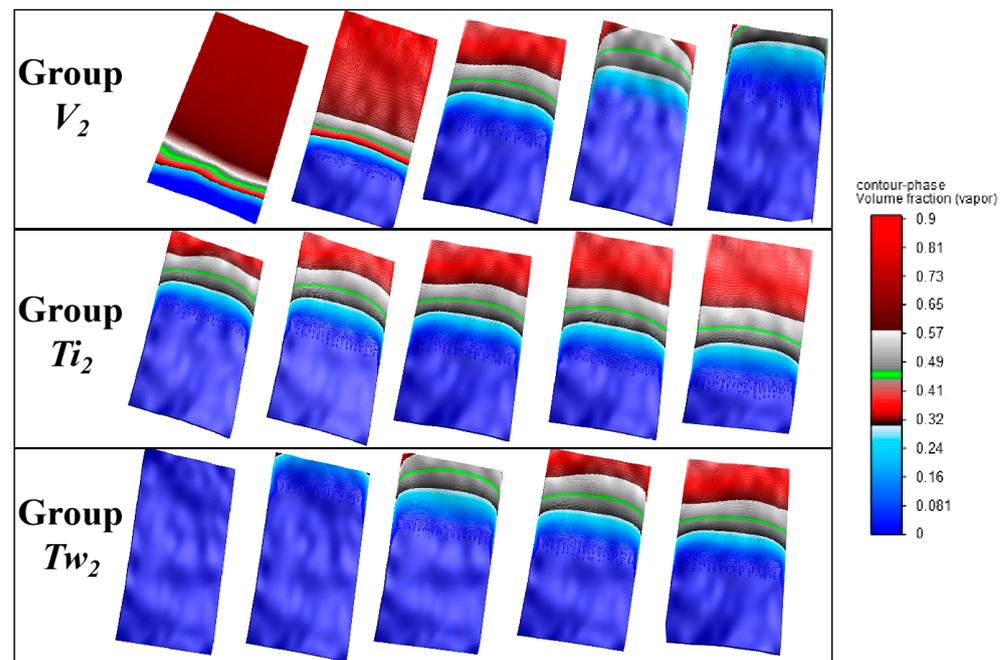
Figure 8. Cloud distribution of water vapor and gas volume percentages in different grouping models.

Figure 9 illustrates the distribution of velocity in the fluid domain, taking conditions V_1–3 and V_2–3 as examples. From the figure, it can be observed that the fluid velocity was 0 m/s at the upper, lower, left, and right wall surfaces, while the inlet velocity was 0.05 m/s; this configuration was consistent with the specified boundary conditions. Observing the velocity along the flow direction, it can be noticed that, at the outlet, it was significantly greater than at the inlet. The model V_1–3, which does not consider the phase transition effect, exhibits an outlet velocity mean and peak values of 0.052 m/s and 0.08 m/s, respectively. In contrast, the model V_2–3, which considered phase transition, showed outlet velocity mean and peak values of 0.186 m/s and 0.3 m/s, respectively. This is because, with the increase in fluid temperature, the density of the fluid began to decrease, leading to the expansion of fluid volume. However, the mass of the fluid entering from the inlet and exiting from the outlet was conserved. Therefore, the volumetric flow rate of the fluid at the outlet began to increase. As for the liquid phase fluid, its density underwent a relatively small change with temperature; hence, the increase in its flow velocity was not significant. However, for the model V_2–3 that considered the effect of fluid phase transition, the vaporization of the liquid phase fluid significantly altered the fluid density, leading to a more than twofold increase in flow velocity.
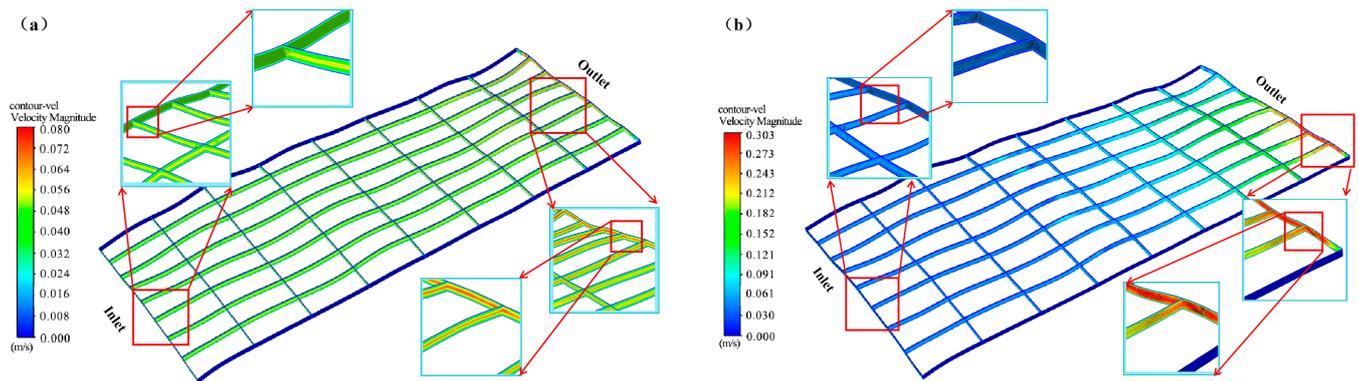
Figure 9. Fluid velocity distribution cloud map. (**a**) Model V_1–3, (**b**) model V_2–3.

Figure 10 depicts the relationship curve between the pressure gradient and flow rate for the V_1, V_2, and Φ group models. In the Φ group of models, as the rock wall temperature was set to the same value as the fluid temperature, there was no heat exchange occurring in this system. From the dashed lines in the graph, it can also be observed that there was a linear relationship between flow rate and pressure gradient at this point. This indicates that without considering heat exchange, the movement of low-flow fluid in the fracture exhibited a well-defined linear relationship. This is consistent with the quantification expressed by Darcy's law. However, when considering the heat exchange effects within the system, the relationship between pressure gradient and flow rate was no longer linear. This further illustrates that heat transfer effects alter the fluid's motion state, making non-linear effects more prone to occur. This is because, in the absence of considering heat transfer effects, the nonlinear effects in the fluid often occur when the fluid has a relatively high velocity. This is also because excessively high velocities can render the inertia term in the Navier–Stokes equations non-negligible. On the contrary, when considering heat transfer effects, nonlinear flow behavior persists even at relatively low velocities. The main reason for this lies in the fact that temperature alters the physical parameters of the fluid, such as density and viscosity.
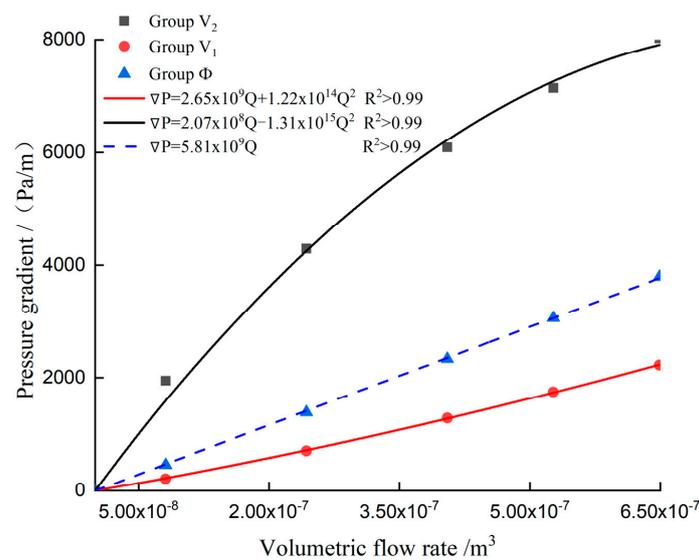
Figure 10. Pressure gradient and flow curves in V_1 group models, V_2 group models, and Φ group models.

Through Figure 10, we can also observe that the phase transition leads to two distinct nonlinear phenomena exhibited by the fluid. When neglecting the phase transition effect of the fluid, under the same flow rate increment, the increment of the pressure gradient was higher than the increment in the linearly increasing case. The curve was convex towards

the flow rate axis. When considering the phase transition effect of the fluid, under the same flow rate increment, the increment of the pressure gradient was lower than the increment in the linearly increasing case. The curve was convex towards the pressure gradient axis. This is because, when not considering phase transition, the fluid moved within the fractures in the liquid phase. At this point, the viscosity of the fluid had a significant impact on its motion. The viscosity of liquid phase water decreased with increasing temperature, but higher flow rates resulted in a decrease in fluid temperature after reaching thermal stability. This led to the need for a larger pressure gradient to achieve the same flow rate increment. When considering the phase transition phenomenon of the fluid, the density of the fluid had a significant impact on the motion of the mixed fluid. Because the process of liquid water converting to gaseous water involves volume expansion, it led to an increase in pressure within the fluid domain. However, as the flow rate increased, the volume of the gaseous phase decreased after heat transfer stabilized within the fluid domain. Therefore, with an equivalent increase in flow rate, a smaller pressure gradient was required.

Furthermore, both types of nonlinear effects caused by heat transfer can be described using the Forchheimer equation. When used to describe the flow state of multiphase fluids, the nonlinear coefficient becomes negative, resembling the behavior of shear-thinning fluids. This also indicates that the resistance experienced by multiphase fluids decreases as the flow velocity increases.

3.2. Heat Transfer Characteristics under Single-Phase and Multiphase Heat–Flow Coupling

Based on Bai's low-temperature seepage and heat transfer experiment, the temperature value of the constant-temperature wall was increased to meet the condition of fluid phase transition. According to Equation (10), the local convective heat transfer coefficient was calculated by taking the fracture profile curve at the center of the model. Figure 11 summarizes the distribution curves of the local convective heat transfer coefficients in different grouping models. The data for Figure 11a, Figure 11b, and Figure 11c are respectively sourced from the V_1 group models with different inlet velocities, the Ti_1 group models with different inlet temperatures, and the Tw_1 group models with different wall temperatures. The common feature among these three groups of models is that they did not take into account the phase transition effect of the fluid. From these three sets of Figure 8, it can be observed that the curves of the local convective heat transfer coefficient exhibited similar trends of increase or decrease at the same positions. Peaks or valleys also appeared at the same positions in each set. This indicates that the inlet velocity, inlet temperature, and wall temperature only affected the magnitude of the local convective heat transfer coefficient, while the distribution of the local convective heat transfer coefficient was controlled by the local roughness of the wall surface. The cause of this phenomenon may be attributed to the calculation principles of the local convective heat transfer coefficient because in the calculation process, we discretized the entire fluid domain with a length of 0.15 mm. However, due to the undulating nature of the fracture surface, within the region of a straight length of 0.15 mm, the fracture surface with more pronounced undulations had a larger actual contact area with the fluid. This phenomenon led to greater heat exchange within the discrete units. Therefore, reflected in the local convective heat transfer curve is the same changing trend at the same location. However, this is also consistent with reality. Many scholars have pointed out in their research that the rougher the fracture surface, the greater the heat exchange [15–17].
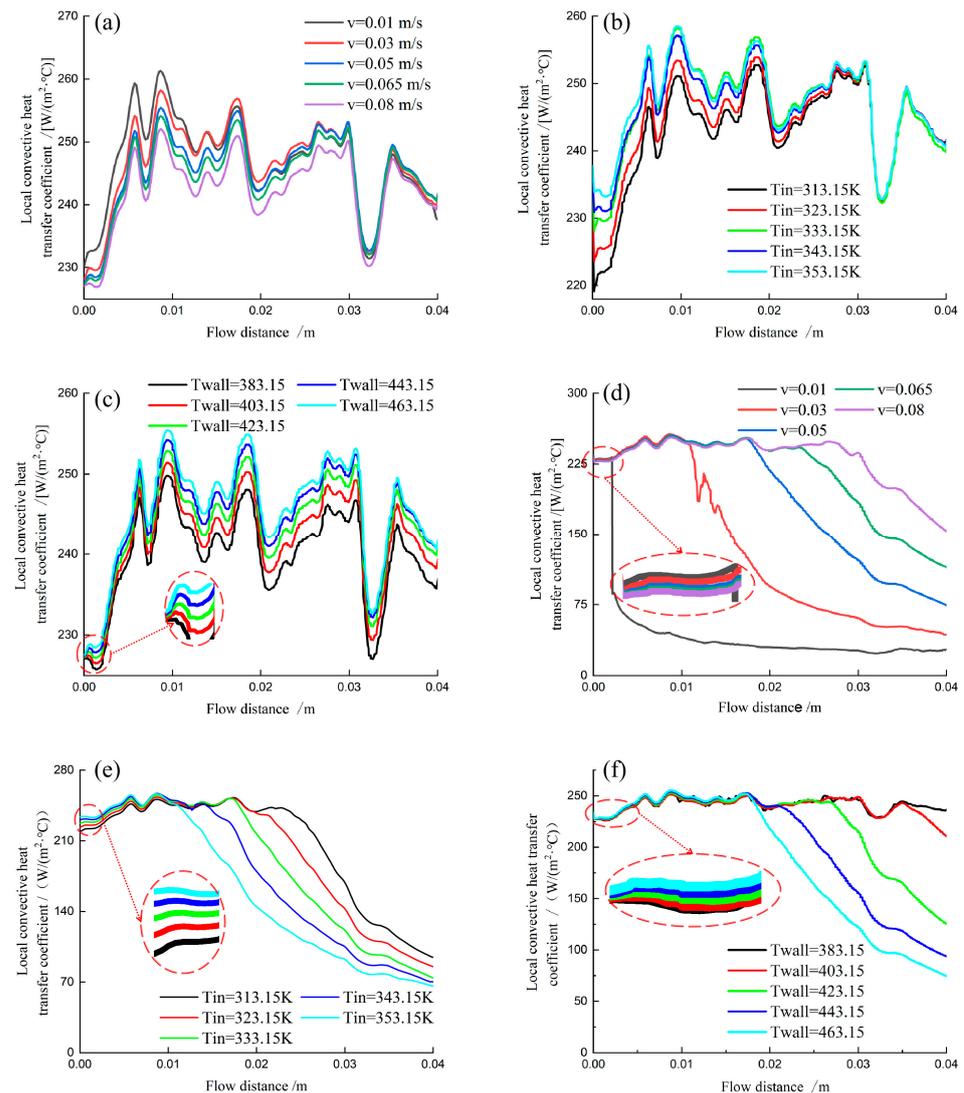
Figure 11. Distribution curve of local heat transfer coefficient along flow direction at different groups: (**a**) group V_1; (**b**) group Ti_1; (**c**) group Tw_1; (**d**) group V_2; (**e**) group Ti_2; (**f**) group Tw_2.

Based on the established single-phase heat–flow coupling model, boiling was introduced into the fluid, causing a phase transition phenomenon when the fluid temperature reached the saturation temperature. As the heating continued, the percentage of liquid phase fluid in the fluid domain decreased, while the percentage of gas phase volume increased. The data for Figure 11d–f are obtained from models with different boundary conditions, taking into account the phase transition effect. It can be observed that in the local area near the inlet, the process of heat transfer was mainly carried out through the liquid phase water. Therefore, the variation pattern of the local convective heat transfer coefficient was similar to those models that did not take into account the phenomenon of phase transitions. For example, within the 1–2 mm range from the inlet, the local heat transfer coefficient increased with a decrease in inlet velocity and an increase in inlet temperature and wall temperature. The stable temperature of model Tw_2–1 did not reach saturation stability and no phase transition occurred, so its local convective heat transfer coefficient was similar to that of model Tw_1–1. This also indirectly reflects the reliability of the multiphase heat–flow coupling model. However, with the increase in flow distance, the distribution characteristics of the local convective heat transfer coefficient underwent significant changes due to the phase transition effect. On the one hand, the fluctuations in the local convective heat transfer coefficient decreased, and the decrease rate was faster

with a lower inlet flow rate and wall temperature and higher inlet temperature. On the other hand, the distribution characteristics of the local convective heat transfer coefficient no longer exhibited strong regularity. This indicates that the phase transition effect changed the fluid heat transfer parameters, thereby causing the local roughness of the fracture to no longer control the distribution characteristics of the local heat transfer coefficient.

To compare the effect of phase transition on heat transfer, the local heat transfer coefficients at the center profile of the model were collected and plotted in Figure 12, using the operating conditions V_1–2 and V_2–2 as examples. From the graph, it can be observed that in the local entrance region, where the fluid had not undergone phase transition, both models V_1–2 and V_2–2 had similar local heat transfer coefficients. However, as the flow distance increased, the volume fraction of vapor phase water gradually increased, leading to fluctuations and reductions in the local heat transfer coefficient of model V_2–2. Furthermore, there was a clear negative correlation between the two variables. From Equation (10), it can also be observed that when the fluid had the same temperature distribution as the rock surface, the magnitude of the local heat transfer coefficient depended on the fluid's physical parameters ($\overline{C}$) and mass flow rate ($\overline{\rho}u\delta$). However, for each cell, mass conservation was observed as mass flowed in and out from the front and rear sections of the cell. Therefore, the magnitude of the specific heat capacity had a significant impact on the local heat transfer coefficient. When considering the phase transition effects, with the increase in gas volume percentage, the specific heat capacity of the mixed fluid became closer to that of gaseous water. This resulted in the phenomenon of the local convective heat transfer coefficient decreasing with the increase in the gas phase volume fraction. From a microscopic perspective, this can also be explained. Because the molecules of gaseous water have a larger intermolecular distance and weaker interaction forces, absorbing the same amount of energy results in faster molecular motion, manifesting as a quicker temperature rise on a macroscopic scale. Additionally, due to the increased flow velocity after fluid vaporization, the reduced heat transfer time in the rock limits the heat transfer capacity of the fluid.
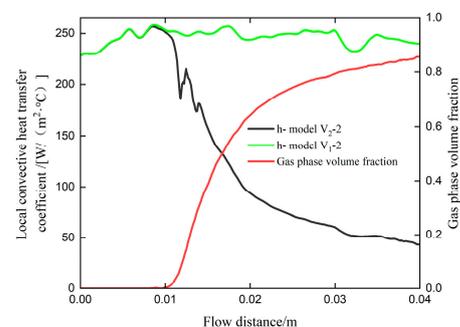
Figure 12. The local heat transfer coefficient and gas volume percentage of V_1–2 and V_2–2 change curves with flow direction.

In order to further quantify the relationship between gas volume percentage and local convective heat transfer coefficients, a dimensionless number *H* was defined to measure the extent of the influence on heat transfer when the fluid underwent phase transition Equation (15). From the equation, it can be observed that as *H* increased, the impact of phase transition on heat transfer became more significant, but this influence was diminishing. Next, we compiled the values of *H* at the midsection under all computed conditions and the corresponding gas volume percentage values at respective positions and then plotted them in Figure 13. From the figure, it can be observed that with the increase in gas volume percentage, the relative impact on the local convective heat transfer coefficient followed an exponential trend. When the gas volume percentage was 1, the local convective heat transfer coefficient without considering phase transition was approximately 10 times greater than when considering phase change effects. This further indicates that when

considering phase transition effects, the gas volume percentage plays a dominant role in the distribution characteristics of the local convective heat transfer coefficient.

$$H = \frac{h_{\sin pas}}{h_{mulpas}} \qquad (15)$$

where $h_{\sin pas}$ is the convective heat transfer coefficient calculated by the single-phase heat–flow coupling model; h_{mulpas} is the convective heat transfer coefficient calculated by the multiphase heat–flow coupling model under the corresponding boundary conditions.
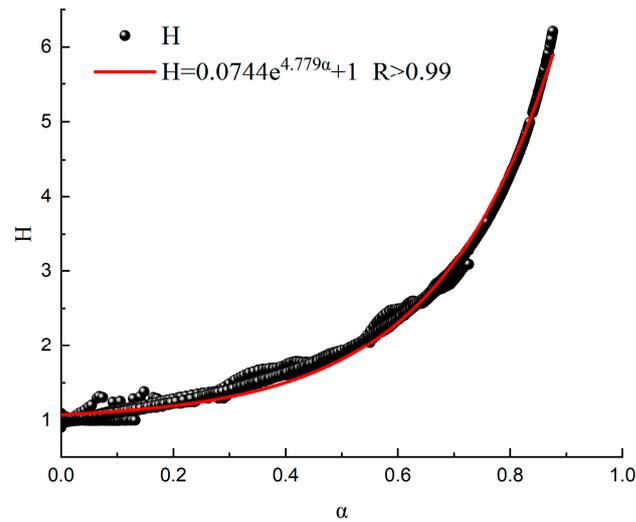
Figure 13. Scatter plot and fitted curve of H and α.

Figure 14 presents the distribution curves of fluid temperature and gas volume percentage, taking scenarios V_1–3 and V_2–3 as examples. From the graph, it can be seen that both had similar temperature distribution curves before the phase transition occurred. As the fluid temperature gradually reached the saturation temperature, neglecting the phase transition effect of the fluid resulted in a steady increase in fluid temperature. However, considering the phase transition effect caused the temperature of the fluid to gradually slow down after reaching the saturation temperature. The reason for this phenomenon is twofold: on the one hand, it is due to the low gas content within this range, and on the other hand, it is because the absorbed heat during the phase transition process is used to overcome intermolecular forces, thereby generating gaseous fluid. By comparing the distribution curves of gas volume percentage, it can be observed that as the phase transition began, the gas volume percentage gradually increased, and the temperature increase rate of the fluid also gradually intensified.
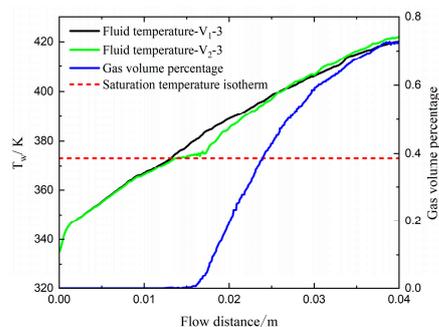
Figure 14. The fluid temperature distribution curves in models V_1–3 and V_2–3.

4. Conclusions

Based on FLURNT 2020 software, single-phase and multiphase heat–flow coupling models were established and the flow–heat transfer characteristics of 3D rough fractures were analyzed. When the phase transition effect was considered or not, the heat–flow coupling mechanism and nonlinear flow mechanism were comparatively studied. The main research results are as follows:

1. In the absence of phase transition effects, the inlet velocity, inlet temperature, and wall temperature only affect the magnitude of the local heat transfer coefficient, of which the distribution characteristics are controlled by the local roughness of the fracture surface. However, when considering phase transition, the distribution characteristics of the local heat transfer coefficient are dominated by the gas phase volume percentage. As the gas content increases, the local heat transfer coefficient decreases.

2. When phase transition of the fluid is not considered, the fluid flow with low flow velocity and no heat transfer effect within the rock wall conforms to Darcy's law. However, when there is heat exchange between the fluid and the rock wall, the nonlinear effects become more significant, and the nonlinear characteristics caused by heat transfer can be described by the Forchheimer equation. After considering phase transition effects, the two-phase fluid exhibits characteristics similar to shear-thinning fluids. Especially under the same pressure gradient, the increment of seepage flow rate is higher than that when linearly increasing. When described using the Forchheimer equation, the nonlinear coefficient is negative.

Author Contributions: Conceptualization, X.L. (Xianshan Liu); Data curation, M.L. and Y.P.; Writing—original draft, X.L. (Xiaolei Luo); Visualization, S.L.; Project administration, P.Z. All authors have read and agreed to the published version of the manuscript.

Funding: TThe research was financially supported by the National Natural Science Foundation of China no. 52279094, no. 41972316 and the Natural Science Foundation Project of CQ CSTB2023NSCQ-MSX0069.

Data Availability Statement: The data presented in this study are available upon request from the corresponding author. The data are not publicly available due to privacy restrictions.

Acknowledgments: The authors acknowledge and appreciate Bai Bing from the Wuhan Institute of Rock and Soil Mechanics, Chinese Academy of Science, for his guidance and help.

Conflicts of Interest: The authors declare that there are no conflicts of interest regarding the publication of this paper. Authors P.Z. and S.L. were employed by the company Communications New Technology Development Company of Shanxi Province. The remaining authors declare that the research was conducted in the absence of any commercial or financial relationships that could be construed as a potential conflict of interest.

References

1. Olasolo, P.; Juárez, M.; Morales, M.; D'amico, S.; Liarte, I. Enhanced geothermal systems (EGS): A review. *Renew. Sustain. Energy Rev.* **2016**, *56*, 133–144. [CrossRef]
2. Wong, K.V.; Tan, N. Feasibility of Using More Geothermal Energy to Generate Electricity. *J. Energy Resour. Technol.* **2015**, *137*, 41201. [CrossRef]
3. Gallup, D.L. Production engineering in geothermal technology: A review. *Geothermics* **2009**, *38*, 326–334. [CrossRef]
4. Liu, J.; Ju, Y.; Zhang, Y.; Gong, W.; Chang, W. Thermal-hydro coupling model of immiscible two-phase flow in heterogeneous porous structures at high temperatures. *Int. J. Therm. Sci.* **2020**, *156*, 106465. [CrossRef]
5. Tan, J.; Rong, G.; He, R.; Yang, J.; Peng, J. Numerical investigation of heat transfer effect on flow behavior in a single fracture. *Arab. J. Geosci.* **2020**, *13*, 851. [CrossRef]
6. Mohais, R.; Xu, C.; Dowd, P. Fluid Flow and Heat Transfer Within a Single Horizontal Fracture in an Enhanced Geothermal System. *J. Heat Transf.* **2011**, *133*, 112603. [CrossRef]
7. Brown, S.R. Fluid flow through rock joints: The effect of surface roughness. *J. Geophys. Res.* **1987**, *92*, 1337–1347. [CrossRef]
8. Tsang, Y.W. The effect of tortuosity on fluid flow through a single fracture. *Water Resour. Res.* **1984**, *20*, 1209–1215. [CrossRef]
9. Li, Z.-W.; Feng, X.-T.; Zhang, Y.-J.; Zhang, C.; Xu, T.-F.; Wang, Y.-S. Experimental research on the convection heat transfer characteristics of distilled water in manmade smooth and rough rock fractures. *Energy* **2017**, *133*, 206–218. [CrossRef]

10. Huang, Y.; Zhang, Y.; Yu, Z.; Ma, Y.; Zhang, C. Experimental investigation of seepage and heat transfer in rough fractures for enhanced geothermal systems. *Renew. Energy* **2019**, *135*, 846–855. [CrossRef]

11. Mandelbrot, B.B. *Fractals: Form, Chance, and Dimension*; W.H. Freeman: San Francisco, CA, USA, 1977.

12. Wang, M.; Chen, Y.-F.; Ma, G.-W.; Zhou, J.-Q.; Zhou, C.-B. Influence of surface roughness on nonlinear flow behaviors in 3D self-affine rough fractures: Lattice Boltzmann simulations. *Adv. Water Resour.* **2016**, *96*, 373–388. [CrossRef]

13. Tian, X.; Ye, Z.Y.; Luo, W. Effect of rock fracture geometry on its seepage and heat transfer characteristics. *Rock Soil Mech.* **2023**, *44*, 1–10.

14. Zhu, Y.; Huang, Y.; Lin, S.; Li, C.; Jiang, P. Experimental study of convection heat transfer characteristics in single rough rock fracture considering multi-level flow rates. *Chin. J. Rock Mech. Eng.* **2019**, *38*, 2654–2667.

15. Tatone BS, A.; Grasselli, G. A method to evaluate the three-dimensional roughness of fracture surfaces in brittle geomaterials. *Rev. Sci. Instrum.* **2009**, *80*, 125110. [CrossRef] [PubMed]

16. He, R.; Rong, G.; Tan, J.; Cheng, L. Numerical investigation of fracture morphology effect on heat transfer characteristics of water flow through a single fracture. *Geothermics* **2019**, *82*, 51–62. [CrossRef]

17. He, Y.; Bai, B.; Hu, S.; Li, X. Effects of surface roughness on the heat transfer characteristics of water flow through a single granite fracture. *Comput. Geotech.* **2016**, *80*, 312–321. [CrossRef]

18. Luo, F.; Xu, R.-N.; Jiang, P.-X. Numerical investigation of fluid flow and heat transfer in a doublet enhanced geothermal system with CO_2 as the working fluid (CO_2–EGS). *Energy* **2014**, *64*, 307–322. [CrossRef]

19. Li, P.; Wu, Y.; Liu, J.; Pu, H.; Tao, J.; Hao, Y.; Teng, Y.; Hao, G. Effects of injection parameters on heat extraction performance of supercritical CO_2 in enhanced geothermal systems. *Energy Sci. Eng.* **2019**, *7*, 3076–3094. [CrossRef]

20. Ma, Y.; Zhang, Y.; Yu, Z.; Huang, Y.; Zhang, C. Heat transfer by water flowing through rough fractures and distribution of local heat transfer coefficient along the flow direction. *Int. J. Heat Mass Transf.* **2018**, *119*, 139–147. [CrossRef]

21. Huang, X.; Zhu, J.; Li, J.; Bai, B.; Zhang, G. Fluid friction and heat transfer through a single rough fracture in granitic rock under confining pressure. *Int. Commun. Heat Mass Transf.* **2016**, *75*, 78–85. [CrossRef]

22. Zhou, G.H.; Wang, J.S. The mechanism by which temperature affects the relative permeability of oil and water. *Acta Pet. Sin.* **1992**, *13*, 62–70.

23. Chen, Y.-F.; Wu, D.-S.; Fang, S.; Hu, R. Experimental study on two-phase flow in rough fracture: Phase diagram and localized flow channel. *Int. J. Heat Mass Transf.* **2018**, *122*, 1298–1307. [CrossRef]

24. Xu, D.; Chen, T.; Xuan, Y. Thermo-hydrodynamics analysis of vapor–liquid two-phase flow in the flat-plate pulsating heat pipe. *Int. Commun. Heat Mass Transf.* **2012**, *39*, 504–508. [CrossRef]

25. Xu, D.; Chen, T.; Liu, X.; Zhang, C.; Hao, Y. Analysis of two-phase flow patterns transition and heat transfer in flat plate loop pulsating heat pipe. *Dong Nan Da Xue Xue Bao J. Southeast Univ.* **2011**, *41*, 558–562.

26. Kiani, K. Nonlocal timoshenko beam for vibrations of magnetically affected inclined single-walled carbon nanotubes as nanofluidic conveyors. *Acta Phys. Pol. A* **2017**, *131*, 1439–1444. [CrossRef]

27. Kiani, K. Nanofluidic flow-induced longitudinal and transverse vibrations of inclined stocky single-walled carbon nanotubes. *Comput. Methods Appl. Mech. Eng.* **2014**, *276*, 691–723. [CrossRef]

28. Kiani, K. Vibrations of fluid-conveying inclined single-walled carbon nanotubes acted upon by a longitudinal magnetic field. *Appl. Phys. A Mater. Sci. Process.* **2016**, *122*, 1038. [CrossRef]

29. Yao, C.; Shao, Y.-L.; Yang, J.-H.; Chen, H.E.; Huang, F.; Zhou, C.-B. Effect of nonlinear seepage on flow and heat transfer process of fractured rocks. *Yantu Gongcheng Xuebao=Chin. J. Geotech. Eng.* **2020**, *42*, 1050–1058.

30. Li, W.L.; Zhou, J.Q.; He, X.L.; Chen, Y.-F.; Zhou, C.-B. Nonlinear flow characteristics of broken granite subjected to confining pressures. *Rock Soil Mech.* **2017**, *38*, 140–150.

31. Liu, R.C.; Jiang, Y.J.; Li, B.; Yu, L.Y.; Du, Y. Nonlinear seepage behaviors of fluid in fracture networks. *Rock Soil Mech.* **2016**, *37*, 2817–2824.

32. Liu, X.; Li, M.; Zeng, N.; Li, T. Investigation on Nonlinear Flow Behavior through Rock Rough Fractures Based on Experiments and Proposed 3-Dimensional Numerical Simulation. *Geofluids* **2020**, *2020*, 8818749. [CrossRef]

33. Xiong, F.; Sun, H.; Jiang, Q.H.; Ye, Z.; Xue, R.; Liu, R. Theoretical model and experimental verification on non-linear flow at low velocity through rough-walled rock fracture. *Rock Soil Mech.* **2018**, *39*, 3294–3302+3312.

34. Hirt, C.W.; Nichols, B.D. Volume of fluid (VOF) method for the dynamics of free boundaries. *J. Comput. Phys.* **1981**, *39*, 201–225. [CrossRef]

35. van Dijk, N.P.; Maute, K.; Langelaar, M.; van Keulen, F. Level-set methods for structural topology optimization: A review. *Struct. Multidiscip. Optim.* **2013**, *48*, 437–472. [CrossRef]

36. Yang, Z.; Peng, X.F.; Ye, P. Numerical and experimental investigation of two phase flow during boiling in a coiled tube. *Int. J. Heat Mass Transf.* **2008**, *51*, 1003–1016. [CrossRef]

37. Lee, W.H. Pressure iteration scheme for two-phase flow modeling. *AIChE Symp. Ser.* **1979**, *1*, 499–501.

38. Gao, X.F.; Zhang, Y.J.; Huang, Y.B. Numerical simulation of convective heat transfer characteristics of a rough single fracture in granite. *Rock Soil Mech.* **2020**, *41*, 1761–1769.

39. Bai, B.; He, Y.; Li, X.; Li, J.; Huang, X.; Zhu, J. Experimental and analytical study of the overall heat transfer coefficient of water flowing through a single fracture in a granite core. *Appl. Therm. Eng.* **2017**, *116*, 79–90. [CrossRef]

40. Chen, Y.; Zhao, Z. Heat transfer in a 3D rough rock fracture with heterogeneous apertures. *Int. J. Rock Mech. Min. Sci.* **2020**, *134*, 104445. [CrossRef]
41. Liu, G.; Zhao, Z.; Chen, Y.; Ma, F.; Wang, G. Comparison between typical numerical models for fluid flow and heat transfer through single rock fractures. *Comput. Geotech.* **2021**, *138*, 104341. [CrossRef]
42. Wang, G.; Liu, G.; Zhao, Z.; Liu, Y.; Pu, H. A robust numerical method for modeling multiple wells in city-scale geothermal field based on simplified one-dimensional well model. *Renew. Energy* **2019**, *139*, 873–894. [CrossRef]
43. Sun, Z.X.; Zhang, X.; Xu, Y.; Yao, J.; Wang, H.X.; Lv, S.; Sun, Z.L.; Huang, Y.; Cai, M.Y.; Huang, X. Numerical simulation of the heat extraction in EGS with thermal-hydraulic-mechanical coupling method based on discrete fractures model. *Energy* **2017**, *120*, 20–33. [CrossRef]
44. Liu, Z.-G.; Zhou, Q.; Yu, L. Density-pressure and density-temperature regression equations of saturated vapour. *J. HVAC* **2001**, *4*, 100–101.